RSC Advances

PAPER

View Article Online
View Journal | View Issue

Cite this: *RSC Adv.*, 2021, **11**, 39287

A novel NIR-II probe for improved tumor-targeting NIR-II imaging†

Chao Hu,‡[a] Tengyu Guo,‡[c] Huizhou Li,[a] Pengfei Xu *[b] and Yudong Xiao*[a]

Received 24th September 2021
Accepted 25th November 2021

DOI: 10.1039/d1ra07135a

rsc.li/rsc-advances

In this work, we report a novel probe IR-RGD, which possesses a bright emission tail in the NIR-II region along with high quantum yield. Further, IR-RGD has been successfully used for tumor-targeting NIR-II fluorescence imaging with great potential for clinical translation.

Introduction

Cancer is a major public health problem worldwide. It is estimated that the deaths induced by cancer may increase by up to 11.0 million in 2030.[1] Cancer continues to present a major, yet unmet challenge to global healthcare. Early diagnosis and efficient therapy are two essential therapy steps for cancer treatment.[2–4] With the rapid development of technology, methods for cancer imaging have been greatly improved over the last decades. Among them, photoinduced imaging modality is attracting increasing attention because it possesses the advantages of high precision and spatiotemporal resolution as well as low radiation and invasion.[5]

Compared with the well-established visible to NIR-I imaging region (400–900 nm), NIR-II biomedical fluorescence imaging in the 1000–1700 nm "second near-infrared (NIR-II) window" has attracted mountainous attentions for tumor imaging. Recent works have demonstrated that light attenuation and scattering as well as background autofluorescence all decrease when imaging in NIR-II region. Thus, NIR-II imaging possess high deep-tissue penetration and spatial resolution properties allowed visualization of deep anatomical features with an unprecedented degree of clarity. So far, the most active materials used for NIR-II imaging are mainly single-walled carbon nanotubes (SWNT), lanthanide nanoparticles, and quantum dots.[6] However, the deficiencies of limited clearance from the body, unknown long-term toxicity, and potential metal ion leakage impede their translation to clinical application.[7–9] Organic fluorophores offer a better alternative and have the most potential for clinical translation because of their designability of physical and optical properties, minimal biotoxicity, *in vivo* biocompatibility, and biodegradation.[10] Recently, Cheng's group demonstrated a pioneering work of designing new type of NIR II organic fluorophores with donor–acceptor–donor (D–A–D) structure.[11] Subsequently, varies D–A–D type NIR-II fluorophores have been explored and be used as NIR II molecular imaging probes.[12–15] However, present D–A–D fluorophores have limited translational potential owing to their own inherent defects. For example, most D–A–D fluorophores are suffering from low quantum yields (QYs), low molar extinction coefficient and poor water solubility.[16,17] Thus, there is great need of NIR II fluorophores with satisfy brightness and biocompatibility for precise tumor imaging.

Interestingly, recent works have demonstrated that NIR-I cyanine dyes revealed long emission tails that extends into the NIR-II region. For example, although the emission spectrum of ICG spans the entire NIR-I region, its fluorescence spectrum exhibits a broad shoulder with a spectral tail extending well into the NIR-II region that can be easily detected by modern InGaAs cameras. Because of this property, NIR-I cyanine dyes can be repurposed for NIR-II bioimaging, thus accelerating the pathway to clinical translation of this imaging modality. Recently, several NIR-I heptamethine cyanine dyes (IR820 and IR783) featured with a rigid chloro cyclohexenyl ring in the methane chain have been used for NIR II fluorescence tumor imaging.[18–21] Such NIR-I dyes will be used much more extensively in NIR-II fluorescence imaging accelerating the pathway to clinical translation of this imaging modality.

As a drug carrier, albumin is playing a vital role for improving the pharmacokinetic profile of peptide and tumor targeting efficacy. In a recent work, Qian and coworkers reported that albumin-binding IR-820 exhibit improving pharmacokinetics, red-shift emission (E_{max} = 858 nm) and enhancement quantum yield (QY = 2.52%).[18] However, it's well known that chlorine group can induce a significant decrease in quantum yields termed as heavy-atom effects.[22–24] Furthermore, albumin-binding IR-820 was engineered to target toward tumor based on the assumed enhanced permeability and retention (EPR) effect in a passive manner, resulting in suboptimal

[a]*Department of Radiology, The Second Xiangya Hospital, Central South University, Changsha, Hunan 410011, P. R. China. E-mail: xiaoyudong222@csu.edu.cn*

[b]*Institute of Clinical Pharmacy & Pharmacology, Jining First People's Hospital, Jining Medical University, Jining 272000, P. R. China. E-mail: pengfeixucsu@outlook.com*

[c]*College of Chemistry Jilin University, Changchun 130012, P. R. China*

† Electronic supplementary information (ESI) available. See DOI: 10.1039/d1ra07135a

‡ These authors contributed equally to this work.

targeting efficacy. Therefore, there is still much room for improvement of the NIR II imaging performance of IR-820.

It has been reported that thiol-substituted IR820 have red-shift absorption/emission and enhancement fluorescence quantum yield, which will benefit for NIR II tumor imaging.[25] In this work, we report a cyclo(RGDfC) decorated IR-820 (termed as **IR-RGD**) for NIR II tumor imaging. Typically, cRGD peptides have been shown to dramatically improve the tumor targeting capability of probes by selectively binding to integrins, a hallmark of cancer.[26,27] In the presence of 10% BSA, the maximum fluorescence peak of **IR-RGD** locate at ~850 nm, which red-shift about 30 nm compared to that of IR-820 in water. It is worth noting that the emission spectrum of **IR-RGD** in 10% BSA could even extend to longer than 1200 nm, and its quantum yield was measured as 3.821%. Based on bright NIR-II tail emission, the whole abdomen vessels and hind limb the vessels were clearly distinguished. Further, **IR-RGD** has been used for tumor-targeting NIR-II fluorescence imaging with great potentials for clinical translation.

Results and discussion

Structure and optical characterization of IR-RGD

As illustrated in Scheme 1, **IR-RGD** was easily synthesized by the reaction of IR-820 and cyclo(RGDfc) in the presence of DIPEA, which was confirmed using MALDI-TOF-MS (expected M.W. 1369.54, measured M.W. 1369.5416). As shown in Fig. 1a, the maximum absorption wavelength of **IR-RGD** in 10% BSA red-shifted to 810 nm. **IR-RGD** in 10% BSA had the maximum fluorescence peak at ~850 nm, which red-shift about 30 nm compared to that of IR-820 in water (Fig. 1b). It is worth noting that the emission spectrum of **IR-RGD** in 10% BSA could even extend to longer than 1200 nm, and its quantum yield in 10% BSA was measured as 3.821% (the QYs of IR-820 is 0.313% in water and 2.52% in 10% BSA).[18] These results verify that **IR-RGD** can act as an ideal contrast agent for NIR II imaging.

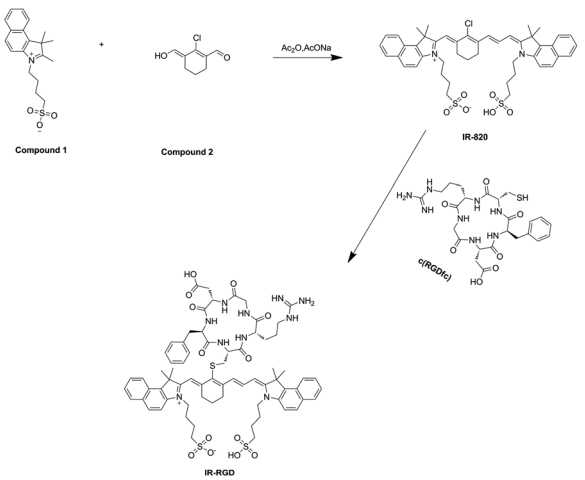

Scheme 1 The synthetic route of IR-RGD.

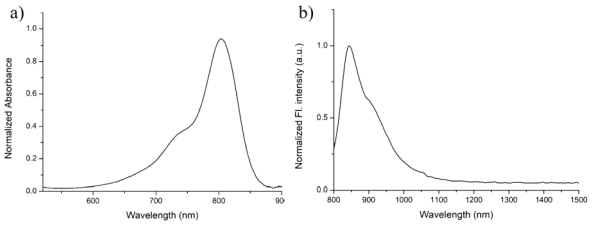

Fig. 1 (a) Normalized absorption spectra of IR-RGD in 10% BSA; (b) normalized PL spectra of IR-RGD in 10% BSA.

In vivo NIR-II fluorescence imaging of hind limb and abdomen vessels

To investigate the potential of **IR-RGD** as a novel NIR-II contrast agent for bioimaging, we injected **IR-RGD** intravenously into BALB/c nude mice at the dose of 2 mg per kg mouse weight. Excitation was achieved using an 808 nm diode laser at 50 mW cm^{-2}, and NIR-II fluorescence images were captured through a 1100 nm LP filter (exposure time, 50 ms). After intravenous injection of **IR-RGD**, the whole abdomen vessels and hind limb the vessels were clearly distinguished (Fig. 2). The high-brightness of **IR-RGD** benefit vessel imaging with enhanced image quality and short exposure time.

In vivo NIR-II fluorescence imaging of tumor

Inspired by above excellent results, we further investigate the potential of **IR-RGD** for the precise detection of tumor. The 4T1 tumor-bearing nude mice were injected with **IR-RGD** *via* tail vein. After intravenous injection of **IR-RGD**, the major blood vessels of the tumor were unambiguously observed. As shown in Fig. 3, the signal intensity in tumor site was gradually enhanced over the course of time. After 24 h, only the tumor region shows strong signal while negligible signal was observed from other organs. This could be attributed to the EPR effect and active targeting mechanism by the high binding efficacy between cRGD and integrins. The SBR at 24 h was calculated to be 28.11(Fig. S7†), which is much higher than that of IR-820 (6.59 at 24 h and 14.72 at 48 h).[18] The excellent imaging result demonstrate that **IR-RGD** offer outstanding promise as a NIR-II probe for aiding tumor localization and intraoperative surgical margin assessment.

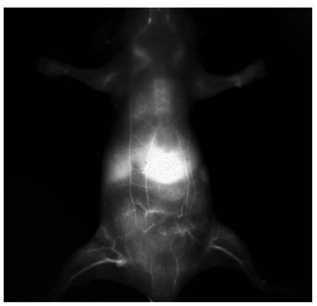

Fig. 2 NIR-II imaging of hind limb and abdomen vessels after injection of IR-RGD.

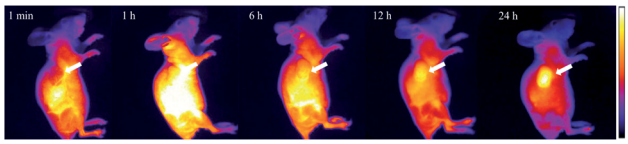

Fig. 3 The *in vivo* NIR-II images of the 4T1 tumor at different time points (1 min to 24 h) after a tail vein injection of IR-RGD.

The signal readings of *ex vivo* organs also indicated that tumors possessed the highest uptake of the **IR-RGD**, followed by kidney and liver (Fig. 4). Other organs showed low organ uptake. The *ex vivo* imaging results indicated that **IR-RGD** could be excreted from the body through hepatobiliary and renal system. Biocompatibility and biosafety are very important for an imaging agent, so we carried out a histological study to evaluate the influence of the **IR-RGD** on living mice. After intravenously injected with **IR-RGD**, the mice were euthanized at 24 h post-injection and major organs were collected for pathology analysis. Hematoxylin and eosin (H&E) stain reveals there were no morphological changes in all the tested organs (Fig. S8†), suggesting good biocompatibility of **IR-RGD**.

Conclusions

NIR-II biological imaging (1000–1700 nm) has shown promise of deep tissue penetration, high spatial resolution, and low background. Among of all the NIR-II probes, organic probes particularly attract mountainous attention due to their excellent stability and biocompatibility. However, most previously reported organic NIR-II fluorescent agents often suffer from low quantum yields in aqueous solution. Herein, we report a cyclo(RGDfC) decorated IR-820 (termed as **IR-RGD**) for NIR II tumor imaging. In the presence of 10% BSA, the emission spectrum of **IR-RGD** could extend to longer than 1200 nm with the maximum fluorescence peak located at ~850 nm. It is worth noting that the quantum yield was measured as 3.821%. Based on bright NIR-II tail emission, noninvasive vessel imaging of limb and abdomen vessels were achieved with high signal-to-background ratio and deep penetration. Further, **IR-RGD** has been used for tumor-targeting NIR-II fluorescence imaging. Collectively, this study demonstrated that **IR-RGD** shows high potentials for clinical translation.

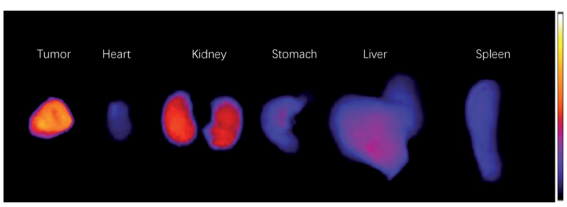

Fig. 4 *Ex vivo* images of main organs of IR-RGD treated mice after 24 h p.i.: tumor, heart, kidney, stomach, liver, and spleen.

Ethical statement

All of the cell and animal studies were approved by the Institutional Animal Care and Use Committee of Jining First People's Hospital (JNRM-2021-DW-017).

Conflicts of interest

There are no conflicts to declare.

Acknowledgements

This work was supported by the National Natural Science Foundation of China (No. 81801813 and 81701754).

Notes and references

1 J. Ferlay, I. Soerjomataram, R. Dikshit, S. Eser, C. Mathers, M. Rebelo, D. M. Parkin, D. Forman and F. Bray, *Int. J. Cancer*, 2015, **136**, E359–E386.
2 S. Laget, L. Broncy, K. Hormigos, D. M. Dhingra, F. BenMohamed, T. Capiod, M. Osteras, L. Farinelli, S. Jackson and P. Paterlini-Brechot, *PLoS One*, 2017, **12**, e0169427–0169476.
3 E. S. V. Souza, L. T. Chinen, E. A. Abdallah, A. Damascena, J. Paludo, R. Chojniak, A. L. Dettino, C. A. de Mello, V. S. Alves and M. F. Fanelli, *OncoTargets Ther.*, 2016, **9**, 7503–7513.
4 H. Wang, N. H. Stoecklein, P. P. Lin and O. Gires, *Oncotarget*, 2017, **8**, 1884–1912.
5 N. Alifu, A. Zebibula, J. Qi, H. Zhang, C. Sun, X. Yu, D. Xue, J. W. Y. Lam, G. Li, J. Qian and B. Z. Tang, *ACS Nano*, 2018, **12**, 11282–11293.
6 S. He, J. Song, J. Qu and Z. Cheng, *Chem. Soc. Rev.*, 2018, **47**, 4258–4278.
7 J. Chen, Y. Kong, W. Wang, H. Fang, Y. Wo, D. Zhou, Z. Wu, Y. Li and S. Chen, *Chem. Commun.*, 2016, **52**, 4025–4028.
8 D. J. Naczynski, M. C. Tan, M. Zevon, B. Wall, J. Kohl, A. Kulesa, S. Chen, C. M. Roth, R. E. Riman and P. V. Moghe, *Nat. Commun.*, 2013, **4**, 2199–2208.
9 S. D. Perrault, C. Walkey, T. Jennings, H. C. Fischer and W. C. Chan, *Nano Lett.*, 2009, **9**, 1909–1915.
10 S. Zhu, B. C. Yung, S. Chandra, G. Niu, A. L. Antaris and X. Chen, *Theranostics*, 2018, **8**, 4141–4151.
11 A. L. Antaris, H. Chen, K. Cheng, Y. Sun, G. Hong, C. Qu, S. Diao, Z. Deng, X. Hu, B. Zhang, X. Zhang, O. K. Yaghi, Z. R. Alamparambil, X. Hong, Z. Cheng and H. Dai, *Nat. Mater.*, 2016, **15**, 235–242.
12 K. Shou, C. Qu, Y. Sun, H. Chen, S. Chen, L. Zhang, H. Xu, X. Hong, A. Yu and Z. Cheng, *Adv. Funct. Mater.*, 2017, **27**, 1700995–1701007.
13 Y. Sun, C. Qu, H. Chen, M. He, C. Tang, K. Shou, S. Hong, M. Yang, Y. Jiang, B. Ding, Y. Xiao, L. Xing, X. Hong and Z. Cheng, *Chem. Sci.*, 2016, **7**, 6203–6207.
14 Q. Yang, Z. Ma, H. Wang, B. Zhou, S. Zhu, Y. Zhong, J. Wang, H. Wan, A. Antaris, R. Ma, X. Zhang, J. Yang, X. Zhang,

H. Sun, W. Liu, Y. Liang and H. Dai, *Adv. Mater.*, 2017, **29**, 1605497–1605506.

15 X. D. Zhang, H. Wang, A. L. Antaris, L. Li, S. Diao, R. Ma, A. Nguyen, G. Hong, Z. Ma, J. Wang, S. Zhu, J. M. Castellano, T. Wyss-Coray, Y. Liang, J. Luo and H. Dai, *Adv. Mater.*, 2016, **28**, 6872–6879.

16 H. Wan, J. Yue, S. Zhu, T. Uno, X. Zhang, Q. Yang, K. Yu, G. Hong, J. Wang, L. Li, Z. Ma, H. Gao, Y. Zhong, J. Su, A. L. Antaris, Y. Xia, J. Luo, Y. Liang and H. Dai, *Nat. Commun.*, 2018, **9**, 1171–1180.

17 Z. H. Lei, C. X. Sun, P. Pei, S. F. Wang, D. D. Li, X. Zhang and F. Zhang, *Angew. Chem., Int. Ed.*, 2019, **58**, 8166–8171.

18 Z. Feng, X. M. Yu, M. X. Jiang, L. Zhu, Y. Zhang, W. Yang, W. Xi, G. H. Li and J. Qian, *Theranostics*, 2019, **9**, 5706–5719.

19 R. Tian, Q. Zeng, S. J. Zhu, J. Lau, S. Chandra, R. Ertsey, K. S. Hettie, T. Teraphongphom, Z. B. Hu, G. Niu, D. O. Kiesewetter, H. T. Sun, X. D. Zhang, A. L. Antaris, B. R. Brooks and X. Y. Chen, *Sci. Adv.*, 2019, **5**, 0672–0683.

20 J. A. Carr, D. Franke, J. R. Caram, C. F. Perkinson, M. Saif, V. Askoxylakis, M. Datta, D. Fukumura, R. K. Jain, M. G. Bawendi and O. T. Bruns, *Proc. Natl. Acad. Sci. U. S. A.*, 2018, **115**, 4465–4470.

21 S. Zhu, Z. Hu, R. Tian, B. C. Yung, Q. Yang, S. Zhao, D. O. Kiesewetter, G. Niu, H. Sun, A. L. Antaris and X. Chen, *Adv. Mater.*, 2018, **30**, 1802546–1802555.

22 J. Eng, S. Thompson, H. Goodwin, D. Credgington and T. J. Penfold, *Phys. Chem. Chem. Phys.*, 2020, **22**, 4659–4667.

23 X. Wang, J. Lv, X. Yao, Y. Li, F. Huang, M. Li, J. Yang, X. Ruan and B. Tang, *Chem. Commun.*, 2014, **50**, 15439–15442.

24 J. Zou, Z. Yin, K. Ding, Q. Tang, J. Li, W. Si, J. Shao, Q. Zhang, W. Huang and X. Dong, *ACS Appl. Mater. Interfaces*, 2017, **9**, 32475–32481.

25 F. Song, X. Peng, E. Lu, Y. Wang, W. Zhou and J. Fan, *Tetrahedron Lett.*, 2005, **46**, 4817–4820.

26 S. Liu, *Bioconjugate Chem.*, 2015, **26**, 1413–1438.

27 J. Yang, Y. Luo, Y. Xu, J. Li, Z. Zhang, H. Wang, M. Shen, X. Shi and G. Zhang, *ACS Appl. Mater. Interfaces*, 2015, **7**, 5420–5428.